The Astrophysical Journal, 998:45 (14pp), 2026 February 10 https://doi.org/10.3847/1538-4357/ae313e

Particle Transport from First Principles in the Early Heliosphere: κ^1 Ceti as a Case Study for the Young Sun

N. Eugene Engelbrecht[1,2], Konstantin Herbst[3], Klaus Scherer[4], Sean Oughton[5], and Vladimir S. Airapetian[6,7]
[1] Centre for Space Research, North-West University, 2520, Potchefstroom, South Africa; n.eugene.engelbrecht@gmail.com
[2] National Institute for Theoretical and Computational Physics (NITheCS), South Africa
[3] Centre for Planetary Habitability (PHAB), Department of Geosciences, University of Oslo, Norway
[4] Ruhr University Bochum, Germany
[5] Department of Mathematics and Statistics, University of Waikato, Hamilton 3240, New Zealand
[6] NASA Goddard Space Flight Center, Greenbelt, MD, USA
[7] American University, Washington, DC, USA
Received 2025 December 3; revised 2025 December 15; accepted 2025 December 24; published 2026 February 3

Abstract

Several studies of Galactic cosmic-ray (GCR) modulation within the astrospheres of stars deemed to be proxies for the young Sun have concluded that the intensities of these particles would, at early stages of the Sun's evolution, be negligible at 1 au. These studies, however, do not take into account the varying interstellar conditions the young Sun would have encountered as it traversed its Galactic orbit, nor do they realistically model the transport of GCRs. The present study, for the first time, examines the influence of various interstellar parameters in the Galactic spiral arms on the astrosphere of κ^1 Ceti, a young Sun proxy, through magnetohydrodynamic modelling. We demonstrate that these conditions lead to an astrosphere with considerably smaller dimensions than previous estimates. We also model the transport of turbulence parameters within said astrosphere for the first time, demonstrating that turbulence levels could be significantly higher than observed in the heliosphere. Finally, these insights are implemented in a 3D, ab initio GCR transport model to compute GCR intensities at 1 au, demonstrating the importance of drift effects in astrospheric modulation: full drift effects lead to GCR intensities comparable to modern observations, while turbulence-reduced drift coefficients lead to significantly smaller intensities.

Unified Astronomy Thesaurus concepts: Astrospheres (107); Solar evolution (1492); Magnetohydrodynamical simulations (1966); Interplanetary turbulence (830); Galactic cosmic rays (567)

1. Introduction

Over the past decades, the discovery of potentially habitable exoplanets orbiting G, K, and M main-sequence stars (see, e.g., A. L. Shields et al. 2016; M. L. Hill et al. 2023) and planned missions that promise the discovery of many more (particularly around Sun-like stars, e.g., J. Kammerer et al. 2022; H. Rauer et al. 2025) have generated considerable scientific, as well as public, interest. It has become increasingly clear that any investigation into the potential habitability of a given exoplanet requires also a comprehensive physics-based study of its ionizing radiation environment, as this can have a significant impact on its atmospheric chemistry and erosion (J. Linsky 2014; V. S. Airapetian et al. 2016, 2017, 2020; J. Hu et al. 2022; K. Poppenhaeger 2022; K. Herbst et al. 2024) and its habitability (e.g., F. Tabataba-Vakili et al. 2016; K. Herbst et al. 2019; M. Scheucher et al. 2020). Recent Kepler and TESS data suggest that magnetically active stars generate frequent and powerful flares that are associated with ejection of coronal material referred to as coronal mass ejections (CMEs; H. Maehara et al. 2012; Y. Notsu et al. 2019; V. S. Airapetian et al. 2020; K. Namekata et al. 2021, 2024a, 2024b, 2025; S. Okamoto et al. 2021; J. R. Callingham et al. 2025; A. M. Veronig et al. 2025). As fast CMEs propagate from stellar coronae into the interplanetary medium, they develop shocks that can accelerate particles to GeV energies via diffusive shock acceleration (G. P. Zank et al. 2000; J. Hu et al. 2022).

As such, in recent years many studies modeling the transport of stellar energetic particles (e.g., F. Fraschetti et al. 2022; D. Rodgers-Lee et al. 2023; N. E. Engelbrecht et al. 2024) and Galactic cosmic rays (GCRs; e.g., K. Herbst et al. 2020; A. L. Mesquita et al. 2021; D. Rodgers-Lee et al. 2021b; K. Herbst et al. 2022; J. Light et al. 2025), have been published, often with varying conclusions as to the intensities, for example, of GCRs at exoplanetary locations, which depend on the models used, and the assumptions made regarding the plasma conditions in the astrospheres of these exoplanets. Realistic multidimensional astrospheric magnetohydrodynamic (MHD) modeling can, however, provide useful inputs to such transport models (K. Herbst et al. 2022), allowing for a self-consistent approach to modeling their plasma properties, which in turn allows for studying charged particle transport in these astrospheres (see, e.g., K. Scherer et al. 2015, 2025; J. Light et al. 2022). The problem of planetary habitability also extends to studies of the space weather of the early Sun and its heliosphere, addressing the early history of our terrestrial habitability by providing insights into planetary formation and possibly the origin and characteristics of prebiotic chemistry and precursor-of-life molecules (see, e.g., M. Güdel 2007; V. S. Airapetian et al. 2016; M. V. Ragulskaya et al. 2018; N. Globus & R. D. Blandford 2020; V. N. Obridko et al. 2020; K. Kobayashi et al. 2023). With a rotation period that was 3–10 times faster than the current Sun, the young Sun's internal magnetic dynamo likely was much more efficient,

generating frequent and energetic flares via magnetic reconnection processes. Several stars have been proposed as astrospheric proxies for the young Sun: EK Dra (HD 129333), π^1 UMa (HD 72905), 47 Cas B (HD 12230), and κ^1 Ceti (HD 20630; e.g., M. Güdel 2007; V. S. Airapetian et al. 2021; K. Namekata et al. 2024a, 2024b). These stars are young, G-type main-sequence stars displaying higher levels of magnetic activity than the current Sun. Studying the transport of GCRs within such proxy astrospheres can provide useful insights into the radiation environments of the early Earth, Venus, and Mars.

Previous studies on the transport of GCRs in young Sun proxy astrospheres all conclude that GCR intensities are expected to be much lower than what is observed in the present day (see H. Svensmark 2006a; O. Cohen et al. 2012; D. Rodgers-Lee et al. 2020, 2021a; S. R. Raeside et al. 2025). These studies, with the exception of O. Cohen et al. (2012), employ 1D solvers for the E. N. Parker (1965) GCR transport equation. Such an approach, while having the benefits of relatively simple implementation, suffers from several limitations, as a 1D approach cannot take into account the 3D complexity of the astrospheric structure implied by global MHD modeling (e.g., A. A. Vidotto et al. 2009; V. S. Airapetian & A. V. Usmanov 2016; V. S. Airapetian et al. 2021; A. A. Vidotto 2021; D. Evensberget et al. 2023; J. Kleimann et al. 2023; K. Scherer et al. 2025). Simplified 1D models also cannot take into account the important 3D transport processes, such as anisotropic diffusion and drift, which are known from heliospheric modulation studies and observations to play an important role in the transport of these particles (see, e.g., J. Kóta 2016; N. E. Engelbrecht & V. Di Felice 2020; N. E. Engelbrecht et al. 2022), and have been demonstrated to greatly influence GCR intensities computed in various astrospheric contexts, leading to different, contradictory conclusions as to GCR intensities at exoplanetary distances from the host stars (see, e.g., N. E. Engelbrecht et al. 2024; J. Light et al. 2025). Uncertainties, however, exist in 3D modeling, which requires a self-consistent modeling of the influence of the stellar environment on GCR intensities, particularly in terms of diffusion and drift coefficients. When modeled from first principles, these also depend on turbulence quantities that cannot yet be ascertained for different astrospheres, let alone the young Sun. Turbulence transport models (TTMs), which have been considerably refined in the past decades within the modern heliospheric context (see, e.g., G. P. Zank et al. 1996; B. Breech et al. 2008; S. Oughton et al. 2011; G. P. Zank et al. 2012, 2017; L. Adhikari et al. 2021; S. Oughton & N. E. Engelbrecht 2021; J. Kleimann et al. 2023; M. A. Bishop et al. 2025; A. V. Usmanov et al. 2025, and references therein), can provide insights into the spatial behavior of turbulence quantities, which can then be used to model diffusion and drift coefficients from first principles. Such diffusion and drift coefficients having also been applied in heliospheric GCR modulation studies, which has resulted in computed GCR intensities in reasonable to good agreement with spacecraft observations (see N. E. Engelbrecht et al. 2022, and references therein).

Prior studies, when estimating the size of the astrospheres of young Sun proxies, have also assumed that the local interstellar medium (LISM) encountered by these astrospheres would be similar to those encountered today, i.e., conditions as are prevalent in the Local Bubble, a cavity in the LISM characterized by a low neutral particle density ($\sim$0.005 particles cm^{-3}, K. Wyman & S. Redfield 2013) formed by supernovae approximately 10–15 million years ago (see, e.g., D. Breitschwerdt & M. A. de Avillez 2006; B. Fuchs et al. 2009; M. M. Schulreich et al. 2018; J. L. Linsky & E. Moebius 2023; A. Youngblood et al. 2025). This, in conjunction with the high mass-loss rates characteristic of young Sun proxies, has understandably lead to very large (usually analytical) estimates for their astrospheric sizes, typically greater than a thousand astronomical units (e.g., D. Rodgers-Lee et al. 2021b; S. R. Raeside et al. 2025). MHD simulations of the heliosphere corroborate this for a range of interstellar parameters, particularly the interstellar neutral hydrogen density, and have shown that smaller neutral densities lead to a larger heliosphere, and vice versa (see, e.g., G. P. Zank & P. C. Frisch 1999; H.-R. Müller et al. 2006, 2009; J. A. Miller & B. D. Fields 2022). As a larger heliosphere has long been known to lead to more modulation of GCRs (and vice versa; K. Scherer et al. 2008; P. C. Frisch & H.-R. Mueller 2013; J. M. Jasinski et al. 2020), such large astrospheres would greatly modulate these particles. However, it is conceivable that the young Sun, as it orbited the Galactic center, would encounter regions of (for example) higher neutral particle densities, particularly within the Galactic spiral arms, as this may have occurred in the recent past when the Local Ribbon of Cold Clouds possibly compressed the heliosphere (M. Opher et al. 2024). Such encounters could reasonably be expected to result in a smaller heliosphere, which in turn could lead to less modulation of the incident GCR local interstellar spectrum (LIS). Additionally, this incident GCR spectrum would also vary throughout the Galaxy (see, e.g., E. Amato & P. Blasi 2018; O. Pezzi & P. Blasi 2024; L. Armillotta et al. 2025), and is expected to be larger within Galactic spiral arm regions than in the interspiral regions (N. J. Shaviv 2002; K. Scherer et al. 2006; H. Svensmark 2006a; I. Büsching & M. S. Potgieter 2008), as these are regions of active star formation (C. Zucker et al. 2022). As the heliosphere traverses such spiral arms with a roughly 150 million year periodicity, such changes may be significant in the long-term evolution of the young Earth's radiation environment.

The aim of this study is to take the abovementioned factors into account by combining (i) state-of-the-art MHD modeling of the astrosphere of κ^1 Ceti in the presence of interstellar conditions corresponding to those expected to be prevalent in the Galactic spiral arms with (ii) turbulence transport modeling within the resulting astrosphere. The star κ^1 Ceti is chosen as it is a relatively well-studied proxy for the young Sun, both observationally as well as with data-constrained MHD simulations of its corona and inner astrosphere (see V. S. Airapetian et al. 2021, and references therein). Turbulence transport modeling, which is here for the first time performed for an astrosphere other than the heliosphere, provides physically motivated turbulence parameters which are then employed in a 3D, ab initio GCR modulation code to realistically model the diffusion and drift coefficients entering into the Parker GCR transport equation so as to calculate GCR proton intensities at 1 au, which can then be compared with modern heliospheric observations.

The paper structure is as follows. The MHD simulations of κ^1 Ceti's greater astrosphere are the subject of the next section, followed by a section devoted to modeling the transport of turbulence parameters within κ^1 Ceti's astrosphere. This is followed by a section introducing the 3D GCR modulation model, and presenting the results so computed. The paper closes with a discussion of the results, as well as the conclusions drawn therefrom.

2. Magnetohydrodynamic Modeling

We use the CRONOS multifluid 3D MHD code (R. Kissmann et al. 2018) to model the astrosphere around κ^1 Ceti as a proxy for that of the young Sun. In this study, only the large-scale structure and fields are simulated, with the behavior of fluctuations treated separately in Section 3. The general set of the Euler equations, which includes the equations of continuity, momentum, and energy, and, in addition, the induction equation for the magnetic field, is given by

$$\frac{\partial}{\partial t}\begin{bmatrix}\rho\\ \rho\,\boldsymbol{u}\\ e\\ \boldsymbol{B}\end{bmatrix} + \nabla\cdot\begin{bmatrix}\rho\boldsymbol{u}\\ \rho\,\boldsymbol{u}\otimes\boldsymbol{u} + \left(P+\frac{B^2}{8\pi}\right)\hat{\mathrm{C8}}I - \frac{\boldsymbol{B}\otimes\boldsymbol{B}}{4\pi}\\ (e+p)\boldsymbol{u} - \frac{\boldsymbol{B}(\boldsymbol{B}\cdot\boldsymbol{u})}{4\pi}\\ \boldsymbol{u}\otimes\boldsymbol{B} - \boldsymbol{B}\otimes\boldsymbol{u}\end{bmatrix} = \begin{bmatrix}S^{\mathrm{c}}\\ \boldsymbol{S}^{\mathrm{m}}\\ S^{\mathrm{e}}\\ \boldsymbol{0}\end{bmatrix}, \tag{1}$$

where ρ, $\boldsymbol{u}$, P, and $\boldsymbol{B}$ are the mass density, the velocity, the thermal pressure, and the magnetic field vector, respectively, and

$$e = \frac{\rho u^2}{2} + \frac{P}{\gamma-1} + \frac{B^2}{8\pi} \tag{2}$$

is the total energy density for an adiabatic index γ, which we take as $5/3$. The terms on the right of Equation (1) describe the source terms for charge exchange, electron impact, and photoionization (for details see K. Scherer et al. 2014).

The above set of equations is employed to describe both the MHD (conducting) fluid, and, setting $\boldsymbol{B} = 0$, the neutral hydrogen fluid.[8] Both fluids are coupled via the terms on the right. This set of equations is integrated in time on a fixed 3D grid with the CRONOS code (R. Kissmann et al. 2018) until a (sufficiently) steady state has been reached. The CRONOS code was successfully applied in a series of publications (for more details see K. Scherer et al. 2025).

The stellar parameters are taken from V. S. Airapetian et al. (2021), while for the interstellar parameters we discuss two different scenarios, labeled Models 1 and 2 in what follows, depending on the local interstellar conditions that the young Sun may have encountered in its Galactic orbit when it was within a Galactic spiral arm. Differences in interstellar neutral density have in the past been demonstrated, through MHD modeling, to influence the size of the heliosphere: smaller interstellar neutral densities lead to a larger heliosphere, and vice versa (see, e.g., G. P. Zank & P. C. Frisch 1999; H.-R. Müller et al. 2006; H. Svensmark 2006b; J. A. Miller & B. D. Fields 2022; M. Opher et al. 2024), with a corresponding effect on GCR transport (e.g., K. Scherer et al. 2008; P. C. Frisch & H.-R. Mueller 2013). In the case of the assumption that the young Sun passed through a spiral arm (K. Herbst 2013), we assume that the Sun moves with a circular Keplerian speed of $v_\odot = 239\,\mathrm{km\,s^{-1}}$ around the Galactic center at a distance of 8.23 kpc (H. W. Leung et al. 2023). Furthermore, the rotation speed of a Galactic arm lies between $\Omega_p \in 30$–$50\,\mathrm{km\,s^{-1}\,kpc^{-1}}$ (A. Castro-Ginard et al. 2021). Thus in Model 1 an interstellar medium (ISM) speed of $v_{\mathrm{ism}} = 50\,\mathrm{km\,s^{-1}}$ gives a moderate value for the relative speed, while in Model 2 we take the extreme case of $v_{\mathrm{ism}} = 150\,\mathrm{km\,s^{-1}}$. We use the ram pressure as $\rho V^2/2$, which leads to a factor of 2 in the total pressure P_{tot} of the ISM, which in general reads (G. P. Zank et al. 2022)

$$P_{\mathrm{tot}} = \frac{\rho V^2}{2} + \frac{1}{2}\frac{\alpha_o B^2}{\mu} + p_{\mathrm{therm}} + p_{\mathrm{GCR}} + p_{\mathrm{dust}} + p_{\mathrm{rad}} + p_{\mathrm{turb}} + \ldots. \tag{3}$$

The terms of the right-hand side of Equation (3) are the ram pressure, magnetic field pressure, thermal pressure, cosmic-ray pressure, and the pressures due to dust, radiation and turbulence. The latter three are usually too small to play a role. The parameter α_o takes care of the obliquity of the magnetic field. The ram, magnetic field, and thermal pressures are usually of the same order. In Table 1 these values, taken from B. T. Draine (2011), are shown. From that table it can be seen that only for ISM speeds larger than 30 km s^{-1} will the ram pressure dominate, while for smaller speeds the other pressure terms are larger or of the same magnitude. One has also to take care regarding ISM parameters, which can be locally different and which can potentially lead to the thermal pressure dominating.

Table 1
The Different Pressure Terms for (Average) Warm Neutral Interstellar Medium Parameters (e.g., B. T. Draine 2011)

Quantity	Value used	Unit
P_{therm}	$n = 0.1\,\mathrm{cm^{-3}}$, $T = 8000$ K	1.1×10^{-13} dyne cm^{-2}
P_B	$B = 3\,\mu$G	3.6×10^{-13} dyne cm^{-2}
P_{GCR}	$=0.25\,\mathrm{eV\,cm^{-3}}$	4×10^{-13} dyne cm^{-2}
P_{ram}	$\rho = 0.1\,\mathrm{cm^{-3}}$, $u = 10\ldots30\ldots100\,\mathrm{km\,s^{-1}}$	$(0.8\ldots7\ldots80)\times10^{-13}$ dyne cm^{-2}

Both models have the problem that, due to computational and memory restrictions and because of the large astrospheres, the resolution is poor. In all models the ram pressure dominates the dynamics inside the termination shock (TS) or in other words the sonic and Alvén Mach numbers are larger than one, and hence the fast magnetosonic Mach number as well. Because in Models 1 and 2 the ram pressure is very large the distances between the TS and the astropause (AP) as well as between the AP and the bow shock (BS) are very small and poorly resolved. The distances between the TS and BS are only a few astronomical units, so that the cosmic-ray flux at the TS can be expected to be almost identical to that in the ISM. In Models 1 and 2 we took a slightly higher temperature than that in Table 1. The models include high speed streams, which are determined by

$$v_{\mathrm{sw}} = v_{\mathrm{sw,0}}\,[1 - 0.5\tanh(\Delta_C[\vartheta - \vartheta_1]) + 0.5\tanh(\Delta_C[\vartheta + \vartheta_2])], \tag{4}$$

where $v_{\mathrm{sw,0}}$ is the slow stellar wind speed, Δ_C is the steepness of the transition, and $\vartheta_{1,2}$ are the transition colatitudes, which are assumed to be equal. The parameter values can be found in

[8] When the word "hydrogen" is used, we refer to neutral hydrogen atoms, while "proton" stands for ionized hydrogen.

Table 2
Input Parameters for the Two Models

	Units	Model 1		Model 2	
		SW [1 au]	ISM	SW [1 au]	ISM
number density (p)	cm^{-3}	267.3	0.6	267.3	0.6
fast speed (p)	km s^{-1}	1236	50	1236	150
slow speed (p)	km s^{-1}	695	⋯	675	⋯
speed (H)	km s^{-1}	⋯	50	⋯	150
δ_t	...	8	⋯	8	⋯
$\vartheta_{1,2}$	deg	35	⋯	35	⋯
"fast" temperature (p)	kK	85	9	85	9
"slow" temperature (p)	kK	40	⋯	40	⋯
temperature (H)	kK	.	9	.	9
magnetic field	nT	15	1.5	15	1.5
φ_B	deg	⋯	150	⋯	150
ϑ_B	deg	⋯	30	⋯	30
Resolutions					
	au^3	6.25 × 6.25 × 6.25		2.08 × 2.08 × 2.08	
		Distances from models			
$TS_{0°}$	au	208		88.5	
$AP_{0°}$	au	252		90.6	
$BS_{0°}$	au	284		92.7	
$TS_{90°}$	au	423		≈155	
$AP_{90°}$	au	477		≈225	
$BS_{90°}$	au	528		≈266	
		Analytic TS distance			
		$B = 0$	$B \neq 0$	$B = 0$	$B \neq 0$
TS_a	au	521	352	173	163

Note. In the left-hand column p and H denote proton and hydrogen, respectively. The rows indicated by $\bullet_{0°}$ give the TS, AP, and BS distances in the nose direction from the corresponding models computed using the CRONOS code, while the rows indicated by $\bullet_{90°}$ give the approximate distance at the poles. The last line gives distances (indicated by TS_a) calculated from analytic formulae (Equations (5) and (6)) with and without magnetic field pressure (see text for details). Note that SW refers to solar wind.

Table 2. In both of these models the remaining ISM parameters are the same, and are listed in Table 3.

The proton densities yielded by Models 1 and 2 are shown in the left and right panels, respectively, of Figure 1, illustrating the very different astrospheres resulting from the differences in ISM parameters (note the different axis lengths). The wavy structure along the TS, AP, and BS is caused by the fact that the distances between the TS, AP, and BS are small and, due to computational limitations, not well resolved. For both models, the TS distance above the poles is larger than that in the ecliptic (see Table 2). Over the poles, the TS distances (423 and 155 au) are much larger than for today's heliosphere (≈90–100 au), with a similar situation in the ecliptic plane for Model 1 (208 au). For Model 2, however, the ecliptic TS distance of 88.5 au is comparable to that of the heliosphere. Intriguingly, both models yield relatively small astrosheaths, particularly in the nose direction. The picture that emerges is one of an irregularly shaped astrosphere that is, in general, still larger than the modern heliosphere, but considerably smaller than prior estimates of the extent of the astrospheres of young Sun proxy stars.

At this point it is useful, as an aside, to revisit the analytic formulae for the TS distances that are often employed in studies of stellar astrospheres (e.g., H. Svensmark 2006a; S. R. Raeside et al. 2025). For two colliding supersonic hydrodynamic winds, Bernouilli's law yields (see E. N. Parker 1963; F. P. Wilkin 2000; K. Scherer et al. 2025)

$$r_{TS} = r_0 \sqrt{\frac{\rho_{sw} V_{sw}^2}{\rho_{ism} u_{ism}^2}} = \sqrt{\frac{\dot{M}_\star V_{sw}}{4\pi \rho_{ism} u_{ism}^2}}, \quad (5)$$

where r_0 is a reference distance with known values of, e.g., the stellar wind speed and density, and $\dot{M}_\star$ the stellar mass-loss rate. For this situation the thermal pressure term can be

Table 3
Boundary Values Assumed at 0.3 au for the Two-component Turbulence Transport Model

Quantity and Units	Sun[a,b]	κ^1 Ceti[a]
Z^2, $km^2\ s^{-2}$	1250, 1600	2000, 2560
W^2, $km^2\ s^{-2}$	350, 2000	560, 3200
λ, au	0.004, 0.015	0.0064, 0.024
l, au	0.004, 0.015	0.0064, 0.024
$\lambda_{c,s}$, au	0.011, 0.011	0.0176, 0.0176
σ_c, none	0.6, 0.8	0.8, 0.8
$\tilde{\sigma}_c$, none	0.6, 0.8	0.8, 0.8

Notes. See text for details.
[a] Ecliptic value, polar value.
[b] Boundary values used for present-day heliosphere, from N. E. Engelbrecht & R. D. T. Strauss (2018).

neglected. However, for MHD fluids or subfast[9] fluids, the pressure term should be retained and one obtains instead

$$r_{TS} = r_0 \sqrt{\frac{\rho_{\rm sw} V_{\rm sw}^2}{\rho_{\rm ism} u_{\rm ism}^2 + 2P_{\rm tot}}}. \tag{6}$$

The bottom row of Table 2 lists the TS distances calculated either by neglecting the magnetic contribution to the pressure (Equation (5)) or by including it (Equation (6)). While the latter approach leads, not unexpectedly, to a consistently smaller estimate for the TS distance, it should be noted that both approaches tend to overestimate the TS distances obtained the full MHD CRONOS simulations. Having estimated the large-scale structure of the astrosphere for these two models, we will now investigate turbulence transport modeling within the astrosphere of κ^1 Ceti.

3. Turbulence Transport

In the previous section we discussed the large-scale structure of the κ^1 Ceti astrosphere. To make accurate assessments of cosmic-ray behavior we also require estimates for quantities characterizing the fluctuations present in the astrosphere as a function of astroradial distance (recall that we are treating this astrosphere as a proxy for the young heliosphere). To obtain these we consider a steady-state TTM. Ideally, the large-scale fields (wind velocity, magnetic field, and density) present in this model would be determined using a dynamical model, such as the one used in the previous section (see also A. V. Usmanov et al. 2016, 2025; T. Wiengarten et al. 2016; J. Kleimann et al. 2023). However, due to computational restrictions, here we instead employ prescribed large-scale fields in the TTM with magnitudes informed by Models 1 and 2 of Section 2. Our choice of TTM is based on the two-component one presented in S. Oughton et al. (2011), updated to include corrections in the length scale equations (see T. Wiengarten et al. 2016; J. Kleimann et al. 2023). Due to the assumptions made in its derivation, notably that the Alfvén speed remains lower than the stellar wind speed, this TTM is strictly applicable to the region within the TS, and is accordingly only applied there. Other TTMs have more recently been proposed in the literature (see, e.g., G. P. Zank et al. 2012, 2017; L. Adhikari et al. 2017, 2021; J. Kleimann et al. 2023; M. A. Bishop et al. 2025, and references therein). In employing the S. Oughton et al. (2011) model, a primary motivation is its ability to reproduce the behavior of two-component turbulence parameters (such as the slab and 2D variances, W^2 and Z^2, respectively, and their corresponding correlation scales, λ and ℓ; see below) reasonably well in the present heliosphere (see, e.g., S. Oughton et al. 2011; N. E. Engelbrecht & R. A. Burger 2013a; T. Wiengarten et al. 2016; N. E. Engelbrecht & R. D. T. Strauss 2018). This model has also been used with some success in GCR modulation studies (see N. E. Engelbrecht & R. A. Burger 2013b, 2015a; N. E. Engelbrecht 2024; J. S. Troskie et al. 2024). The equations of the steady-state TTM, solved following N. E. Engelbrecht & R. D. T. Strauss (2018), are given by (the prescribed large-scale "background" fields are discussed below Equation (12))

$$\begin{aligned}
\frac{dZ^2}{dr} &= -[1 + M\sigma_D - C_{\rm sh}^Z]\frac{Z^2}{r} - \frac{\alpha f}{V_{\rm sw}}\frac{Z^3}{l} \\
&\quad - \frac{2\alpha f_{ZW}^+}{V_{\rm sw}}\frac{WZ^2}{l}\frac{1}{1 + Z/W} + \frac{2\alpha X^+}{V_{\rm sw}}, \\
\frac{dW^2}{dr} &= -[1 + M\tilde{\sigma}_D - C_{\rm sh}^W]\frac{W^2}{r} - \frac{\tilde{\alpha}\tilde{f}}{V_{\rm sw}}\frac{ZW^2}{\lambda}\frac{2}{1 + \lambda/l} \\
&\quad - \frac{2\tilde{\alpha}(1 - \tilde{\sigma}_c^2)}{V_{\rm sw}}\frac{W^4\lambda_{c,s}}{\lambda^2 V_A} - \frac{2\alpha X^+}{V_{\rm sw}} + \frac{\dot{E}_{PI}}{V_{\rm sw}}, \\
\frac{dl}{dr} &= -\hat{C}_{\rm sh}^z\frac{l}{r} + \underbrace{\frac{l\sigma_D M}{r}} + \frac{\beta}{V_{\rm sw}} \\
&\quad \times \left[fZ + f_{ZW}^+\frac{2W}{1 + Z/W} - \frac{2lX^+}{Z^2}\right], \\
\frac{d\lambda}{dr} &= -\hat{C}_{\rm sh}^W\frac{\lambda}{r} + \frac{\widehat{\lambda\sigma_D M}}{r} + \frac{2\tilde{\beta}}{V_{\rm sw}} \\
&\quad \times \left[\frac{\tilde{f}Z}{1 + \lambda/l} + (1 - \tilde{\sigma}_c^2)\frac{W^2\lambda_{c,s}}{\lambda V_A} + \frac{\alpha\lambda X^+}{\tilde{\alpha}W^2}\right], \\
\frac{d\lambda_{c,s}}{dr} &= -\hat{C}_{\rm sh}^W\frac{\lambda_{c,s}}{r} + 2\tilde{\alpha}(1 - \tilde{\sigma}_c^2) \\
&\quad \times \frac{W^2\lambda_{c,s}^2}{V_{\rm sw}V_A\lambda^2} - (\lambda_{c,s} - \lambda_{\rm res})\frac{\dot{E}_{PI}}{V_{\rm sw}W^2}, \\
\frac{d\sigma_c}{dr} &= \frac{\alpha}{V_{\rm sw}}\left[\frac{f'Z}{l} + \frac{f'_{ZW}W}{l}\frac{2}{1 + Z/W}\right. \\
&\quad \left. - \frac{2(\sigma_c X^+ - X^-)}{Z^2}\right] - \left[\frac{C_{\rm sh}^Z - M\sigma_D}{r}\right]\sigma_c, \\
\frac{d\tilde{\sigma}_c}{dr} &= \frac{2\tilde{\alpha}}{V_{\rm sw}}\left[\frac{\tilde{f}'}{1 + \lambda/l}\frac{Z}{\lambda} + \tilde{\sigma}_c(1 - \tilde{\sigma}_c^2)\frac{W^2\lambda_{c,s}}{\lambda^2 V_A}\right] \\
&\quad + \frac{2\alpha(\tilde{\sigma}_c X^+ - X^-)}{V_{\rm sw}W^2} \\
&\quad - \left[\frac{C_{\rm sh}^W - M\tilde{\sigma}_D}{r} + \frac{\dot{E}_{PI}}{V_{\rm sw}W^2}\right]\tilde{\sigma}_c,
\end{aligned} \tag{7}$$

where the terms $f_{z/w}^{\pm}$ are given by (S. Oughton et al. 2011)

$$\begin{aligned}
f = f_{zz}^+, \quad \tilde{f} &= f_{wz}^+, \\
f' = \sigma_c f_{zz}^+ - f_{zz}^-, \\
\tilde{f}' = \tilde{\sigma}_c f_{wz}^+ - f_{wz}^-, \\
f'_{zw} = \sigma_c f_{zw}^+ - f_{zw}^-,
\end{aligned}$$

with, replacing z and w with symbols a and b

$$f_{ab}^{\pm} = \frac{1}{2}[(1 + \sigma_c^a)\sqrt{1 - \sigma_c^b} \pm (1 - \sigma_c^a)\sqrt{1 + \sigma_c^b}]. \tag{8}$$

The $X^{\pm} = (Y^+ \pm Y^-)/2$ terms model the exchange of energy between the W and Z components, where

$$\begin{aligned}
Y^{\pm} = W_{\pm}Z_{\pm}\left[\frac{Z_{\mp}}{\lambda}\Gamma_w^{z_{\mp}w_{\pm}} + \frac{W_{\mp}}{\lambda}\Gamma_w^{w_{\mp}w_{\pm}}\right. \\
\left. - \frac{Z_{\mp}}{l}\Gamma_w^{z_{\mp}z_{\pm}} - \frac{W_{\mp}}{l}\Gamma_w^{w_{\mp}z_{\pm}}\right],
\end{aligned} \tag{9}$$

[9] Subfast means either subsonic (in hydrodynamics) or subfast magnetosonic (in MHD).

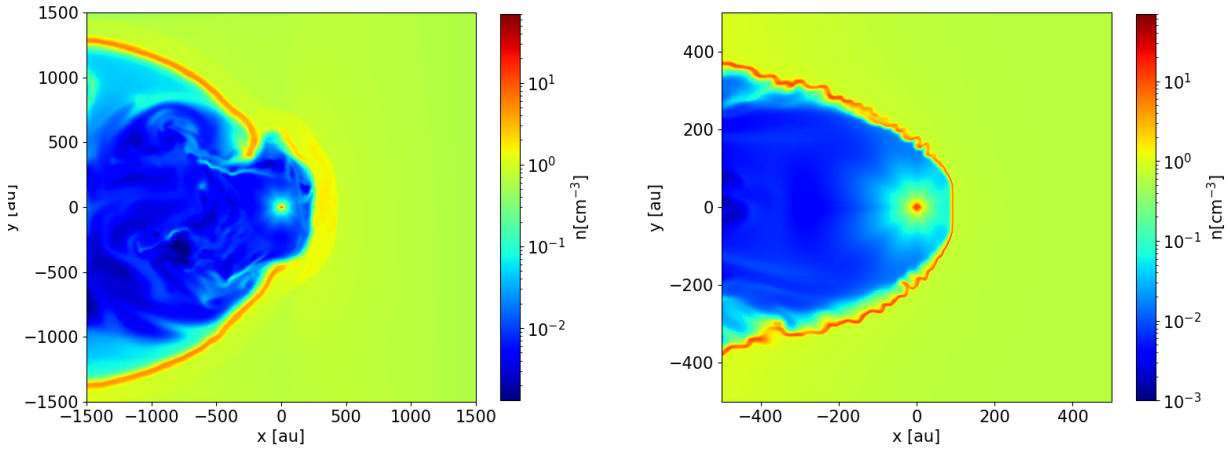

Figure 1. Proton density yielded by the CRONOS multifluid code in the x–y plane for κ^1 Ceti, for Model 1 (left panel) and Model 2 (right panel). Note the different box scales for the left and right panels. See text for details.

and the Elsässer energies are $Z_\pm^2 = Z^2(1 \pm \sigma_c)$ and $W_\pm^2 = W^2(1 \pm \tilde{\sigma}_c)$. Lastly

$$\Gamma_c^{ab} = \frac{1}{1 + \tau_{\rm nl}^{ab}/\tau_A^c}, \tag{10}$$

where $\tau_{\rm nl}^{ab}$ is the nonlinear time, and τ_A^c is the Alfvén time, given by S. Oughton et al. (2006, 2011) as

$$\tau_A^w = \frac{\lambda_{c,s}}{V_A}, \quad \tau_{\rm nl}^{ww} = \frac{\lambda}{W},$$
$$\tau_{\rm nl}^{zz} = \frac{l}{Z}, \quad \tau_{\rm nl}^{zw} = \frac{\lambda}{Z}, \quad \tau_{\rm nl}^{wz} = \frac{l}{W},$$

where V_A denotes the Alfvén speed.

The first two equations of the TTM model the outward evolution of the quasi-2D and wavelike fluctuation energies (Z^2 and W^2) as a function of heliocentric radial distance, subject to various source terms such as shear-driving effects (governed by the $C_{\rm sh}$ terms, here modeled following B. Breech et al. 2008), geometric mixing (modeled, since the fluctuations are assumed to be polarized transverse to $\boldsymbol{B}$, by $M = \cos^2\psi$, with ψ the magnetic field winding angle; W. H. Matthaeus et al. 1994; G. P. Zank et al. 1996; B. Breech et al. 2008), and parallel-propagating wave generation due to the formation of pickup ions (see, e.g., L. L. Williams & G. P. Zank 1994; P. A. Isenberg et al. 2003; modeled by the $\dot{E}_{PI}$ term). In the present study, this last driving effect is neglected for the cases considered below, as fluctuations generated at the frequencies concerned are not expected to play a significant role in GCR proton scattering (N. E. Engelbrecht 2017). However, it is employed in the heliosphere comparison solutions discussed below. Furthermore, the de Kàrmàn–Taylor constants (see S. Oughton & N. E. Engelbrecht 2021, and references therein), related by $\alpha = 2\beta = 0.125$ are chosen following C. Pei et al. (2010), and the normalized energy difference $\sigma_D = -1/3$, in line with modern heliospheric observations (e.g., D. A. Roberts et al. 1987; S. Perri & A. Balogh 2010; M. Iovieno et al. 2016; L. Adhikari et al. 2017). This implies that the Alfvén ratio $r_A = (1 + \sigma_D)/(1 - \sigma_D) = 1/2$. Magnetic variances corresponding to the fluctuation energies can then be calculated from (e.g., B. Breech et al. 2008)

$$\delta B_{2D}^2 = \frac{\mu_o \rho}{1 + r_A} Z^2, \quad \delta B_s^2 = \frac{\mu_o \rho}{1 + r_A} W^2, \tag{11}$$

where ρ denotes the stellar wind proton number density. The S. Oughton et al. (2011) model also solves for various correlation scales: λ and l represent perpendicular correlation scales related to W^2 and Z^2 fluctuations, respectively, while $\lambda_{c,s}$ represents a parallel correlation scale corresponding to the W^2 fluctuations. Note that the equations for these quantities as given above each contain a new term (indicated with an under- or overbrace) due to a correction to the model discussed in Appendix B of J. Kleimann et al. (2023), as well as by M. A. Bishop et al. (2025), resulting in modified mixing terms $\lambda\sigma_D M/r$ and $l\sigma_D M/r$ in the equations for λ and l, respectively, that are not to be found in the original S. Oughton et al. (2011) model. The influence of these terms on solutions to this TTM will be discussed below. As they may not be separately observable it is useful to combine the perpendicular scales in a center-of-mass-type average (S. Oughton et al. 2011):

$$\lambda_{c,2D} = \frac{Z^2 l + W^2 \lambda}{Z^2 + W^2}. \tag{12}$$

The normalized cross helicities σ_c and $\tilde{\sigma}_c$ associated with the Z^2 and W^2 fluctuations are also solved for here, as a matter of completeness, but do not enter into the diffusion coefficients employed in this study. We note that, with additional equations to be solved, the S. Oughton et al. (2011) TTM can also yield proton and electron temperatures (see N. E. Engelbrecht & R. D. T. Strauss 2018); however, these are not solved for herein.

Equations (7) are solved using a fourth-order Runge–Kutta method. Unfortunately, since the associated step-size requirements are much stricter than those used in the large-scale CRONOS MHD simulations of the whole astrosphere (Section 2), outputs from those simulations (e.g., stellar wind density, speed, and astrospheric magnetic field magnitude) are too coarse to be of direct use in the TTM. So, we instead employ analytical models for the needed large-scale plasma quantities[10] normalized to values appropriate to the astrosphere. A similar

[10] For applications where TTMs are directly coupled with MHD codes in the heliospheric context, see, e.g., A. V. Usmanov et al. (2012, 2016, 2025), T. Wiengarten et al. (2016), and J. Kleimann et al. (2023).

approach was followed in N. E. Engelbrecht & R. D. T. Strauss (2018). For the background astrospheric magnetic field, an E. N. Parker (1958) model is assumed, as this is in line with our CRONOS simulation results. This field, normalized to a value of $B_0 = 15$ nT at 1 au following the results in the previous section, as well as those presented by V. S. Airapetian et al. (2021), is given by

$$\boldsymbol{B}(r, \theta) = AB_0 \left(\frac{r_0}{r}\right)^2 (\boldsymbol{e}_r - \tan\Psi \boldsymbol{e}_\varphi), \tag{13}$$

representing spiral magnetic field lines, where A is the polarity and $\boldsymbol{e}_{r,\varphi}$ are the unit vectors in the r and φ directions. The winding angle is given by

$$\tan\Psi = \frac{\Omega(r - r_s)\sin\theta}{V_{\rm sw}}, \tag{14}$$

with Ω the stellar rotation frequency, calculated using the reported rotation period of 9.2 days for κ^1 Ceti, within the range of observations reported by, e.g., S. M. Rucinski et al. (2004) and J. D. do Nascimento et al. (2016), although, for simplicity, reported differential rotation is not taken into account here. To do so would invoke more complicated magnetic field models, such as Fisk-type fields (see, e.g., L. A. Fisk 1996; P. J. Steyn & R. A. Burger 2020), which are considerably more complicated to implement in GCR transport studies (e.g., J. S. Troskie et al. 2024), and do not greatly influence the results of this TTM. For the stellar wind speed, the same latitudinal profile as implemented in the previous section is employed, without a radial dependence, which is a reasonable assumption as the TTM is only to be solved within the TS radius, which is taken from the results of the MHD (CRONOS) modeling. The stellar wind proton density is modeled using an r^{-2} radial profile, normalized to a number density of 267.3 cm^{-3} at 1 au following V. S. Airapetian et al. (2021).

The inner boundary for the model is chosen at 0.3 au, following heliospheric studies. The choice of boundary values for the TTM presents some difficulty, as appropriate values are difficult to glean from observations (as opposed to the case for the present-day heliosphere, where direct spacecraft observations are available). As a point of departure, boundary values that yield results for turbulence parameters in reasonable agreement with spacecraft observations in the modern heliosphere (see, e.g., N. E. Engelbrecht & R. D. T. Strauss 2018) are employed, as listed in the second column of Table 3. These are then modified subject to certain assumptions. A first approach would be to scale the heliospheric inner boundary conditions with some observationally motivated factor. V. S. Airapetian et al. (2021) report on a turbulent wave velocity from an observational estimate of the amplitude of low-frequency Alfvén waves in the chromosphere of κ^1 Ceti that is ≈1.6 times greater than that observed for the modern Sun. In order to take into account this higher-turbulence scenario, the heliospheric inner boundary values for fluctuation energies and correlation scales are hence multiplied by this factor (see the third column of Table 3). High-latitude boundary conditions are scaled up or down with the latitudinal stellar wind speed profile, motivated by heliospheric observations of the fast solar wind (e.g., R. J. Forsyth et al. 1996; B. Bavassano et al. 2000a, 2000b), as discussed by N. E. Engelbrecht & R. A. Burger (2013a). For simplicity, inner boundary conditions for σ_c and $\tilde{\sigma}_c$ (the quasi-2D and wavelike normalized cross helicities) are set equal to the heliospheric high-latitude value of 0.8, reflecting the higher activity levels of κ^1 Ceti, and also kept constant as function of latitude.

The left panels of Figure 2 show heliospheric solutions of the TTM computed both with the new term (solid lines) and without (dotted lines). The additional terms in the equations for l and λ only lead to small differences in the resulting variances and correlation scales, and thus are not expected to greatly influence the conclusions of prior modulation studies performed using turbulence inputs from the original S. Oughton et al. (2011) TTM. However, it should be noted that inclusion of the new terms does lead to larger differences in the normalized cross helicities yielded by this TTM, particularly within 10 au. These quantities, however, do not enter into the calculations of transport coefficients used in modulation studies. The right panels of Figure 2 show the turbulence quantities yielded by the S. Oughton et al. (2011) TTM for the the κ^1 Ceti boundary values as function of radial distance out to 208 au, the TS distance yielded by Model 1. Also shown, to guide the eye and provide a sense of proportion, are heliospheric solutions to the TTM (solid lines), alongside a selection of heliospheric observations. Note that the heliospheric solutions include the contribution of pickup-ion-generated turbulence, while the solutions for κ^1 Ceti do not. This omission is made because the high-frequency fluctuations so generated (see L. L. Williams & G. P. Zank 1994) are not expected to influence particle transport coefficients at the GCR energies considered here (e.g., N. E. Engelbrecht 2017). The top panels of Figure 2 show magnetic variances as function of radial distance. At the smallest radial distances shown, all sets of solutions display a monotonic decrease with radial distance, which for the modern heliosphere are somewhat less steep than for the κ^1 Ceti solutions. Beyond ∼5 au, the heliospheric wavelike variance flattens out due to the contribution of the pickup-ion source term, a behavior not seen for the high- and low-turbulence scenarios due to the omission of said term. At 1 au, the TTM yields a variance of ≈713 nT^2 for κ^1 Ceti, considerably higher than the ≈12 nT^2 value observed in the modern heliosphere (e.g., C. W. Smith et al. 2006), even taking into account the observed solar cycle dependence of this quantity (e.g., L. L. Zhao et al. 2018; R. A. Burger et al. 2022). Variance values for κ^1 Ceti remain consistently high relative to those for the modern heliosphere at larger radial distances. Modern heliospheric quasi-2D correlation scales (middle panels of Figure 2), as well as for the κ^1 Ceti solutions, increase monotonically with radial distance, with the latter cases yielding higher values for this quantity at 1 au. This behavior also holds true, at smaller radial distances, for the radial dependences of the wavelike correlation scales. In the heliospheric case, the pickup-ion term leads to a decrease beyond ∼5 au, whereas the κ^1 Ceti case yields increasing radial dependences at higher radial distances. Finally, normalized cross helicities for κ^1 Ceti (bottom panels of Figure 2) decrease steadily with radial distance, similar to the modern heliospheric solutions.

4. Galactic Cosmic-Ray Modulation

4.1. The Numerical Modulation Model

GCR intensities are here computed using the 3D stochastic solver of the E. N. Parker (1965) cosmic-ray transport equation

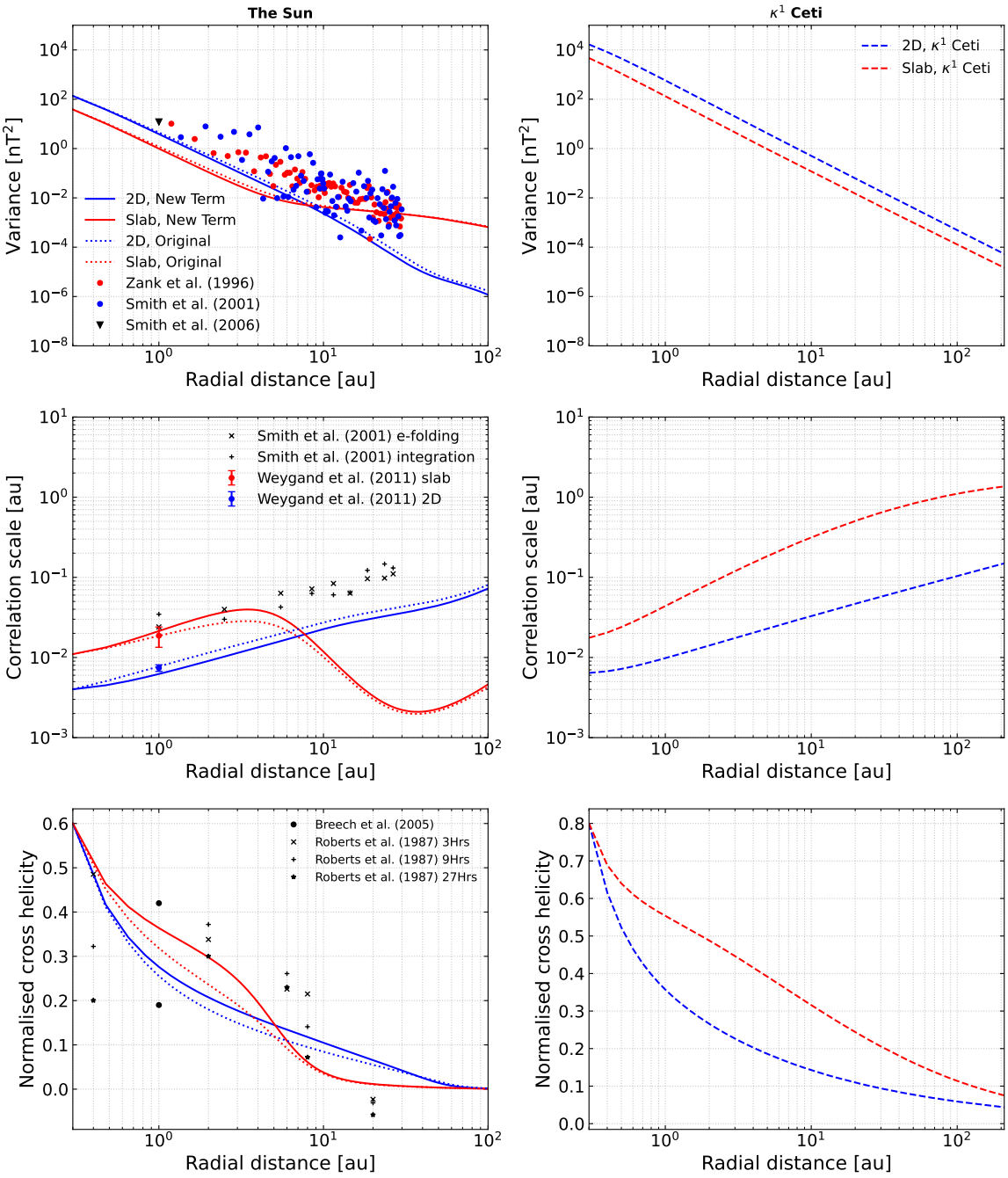

Figure 2. Outputs yielded by the TTM for the heliosphere (left panels) and for κ^1 Ceti (right panels), showing magnetic variances (top panels), correlation scales (middle panels), and normalized cross helicities (bottom panels) as function of radial distance in the ecliptic plane. Solid lines in the left panels indicate heliospheric solutions from N. E. Engelbrecht & R. D. T. Strauss (2018) and dotted lines those calculated with the new term (see text for details). Symbols denote heliospheric observations reported by G. P. Zank et al. (1996), C. W. Smith et al. (2001, 2006), W. H. Matthaeus et al. (1999), J. M. Weygand et al. (2009, 2011), D. A. Roberts et al. (1987), and B. Breech et al. (2005).

employed by N. E. Engelbrecht et al. (2024), given by

$$\frac{\partial f}{\partial t} = \nabla \cdot (\overset{\text{C8}}{\boldsymbol{K}} \cdot \nabla f) - \boldsymbol{V}_{\rm sw} \cdot \nabla f + \frac{1}{3}(\nabla \cdot \boldsymbol{V}_{\rm sw}) \frac{\partial f}{\partial \ln p}, \quad (15)$$

where $f(\boldsymbol{r}, p, t)$ is the omnidirectional cosmic-ray phase space density, $\overset{\text{C8}}{\boldsymbol{K}}$ is the GCR diffusion tensor (see, e.g., R. A. Burger et al. 2008), $\boldsymbol{V}_{\rm sw}$ is the solar or stellar wind speed, and p is the GCR momentum. For more details on this modulation code, as well as on the stochastic method of solving the Parker equation, the reader is invited to consult N. E. Engelbrecht & R. A. Burger (2015a), R. D. T. Strauss & F. Effenberger (2017), K. D. Moloto et al. (2019), and J. Light et al. (2025). The use of a 3D code, while introducing more variables, allows for a more self-consistent modeling of GCR transport (see, e.g., N. E. Engelbrecht & V. Di Felice 2020; J. Light et al. 2025), particularly transport phenomena such as drifts, which cannot be modeled in 1D. For the elements of the diffusion tensor, a combination of quasilinear theory (QLT; see J. R. Jokipii 1966; A. Teufel & R. Schlickeiser 2003) and

nonlinear guiding center (NLGC) theory (see W. H. Matthaeus et al. 2003; A. Shalchi et al. 2004) parallel and perpendicular mean free paths (MFPs) are employed, where the MFP is related to the diffusion coefficient by $\kappa_{\parallel/\perp} = v\lambda_{\parallel/\perp}/3$ (with v the particle speed; A. Shalchi 2009). Given the number of expressions for these quantities derived from several different theories in the literature (see, e.g., A. Shalchi 2009; N. E. Engelbrecht et al. 2022), this choice is motivated by the relatively successful use of QLT and NLGC diffusion coefficients in cosmic-ray modulation studies (see, e.g., K. D. Moloto et al. 2018; N. E. Engelbrecht & K. D. Moloto 2021), as well as their relative tractability. Turbulence quantities yielded by the TTM discussed in the previous section are used directly in the GCR modulation code as inputs for these expressions, under the assumption that quasi-2D and wavelike quantities provide reasonable approximations for 2D and slab turbulence parameters in a stellar wind with a "background" magnetic field (see, e.g., S. Oughton et al. 2011; S. Oughton & N. E. Engelbrecht 2021). There is thus a direct connection between the turbulence transport results and the computed GCR intensities via their transport coefficients, which directly depend upon turbulence quantities computed using the TTM discussed above.

The QLT parallel MFP is derived for a slab turbulence power spectrum with a wavenumber-independent energy range, and an inertial range with a spectral index $-s$, and is given by

$$\lambda_{\parallel} = \frac{3s}{(s-1)}\frac{R^2}{k_m}\frac{B_0^2}{\delta B_{\rm sl}^2}\left[\frac{1}{4\pi} + \frac{2R^{-s}}{\pi(2-s)(4-s)}\right], \quad (16)$$

where $R^2 = R_L/k_m = R_L\lambda_s$ is a function of the maximal Larmor radius R_L and the length scale λ_s at which the inertial range commences, here modeled to first order using the wavelike correlation scale yielded by the TTM discussed in Section 3. At high rigidities P, this quantity displays a P^2 dependence, while at low rigidities, for a Kolmogorov ($s = 5/3$) inertial range, a $P^{1/3}$ dependence. The perpendicular MFP is derived assuming the same form for the 2D turbulence power spectrum as for the slab, with an inertial range spectral index of 2ν, such that (R. A. Burger et al. 2008)

$$\lambda_{\perp} = \left[{\alpha_{\perp}}^2\sqrt{3\pi}\frac{2\nu-1}{\nu}\frac{\Gamma(\nu)}{\Gamma(\nu-1/2)}\lambda_{2D}\frac{\delta B_{2D}^2}{B_0^2}\right]^{2/3}\lambda_{\parallel}^{1/3}, \quad (17)$$

where λ_{2D} is the onset length scale for the 2D inertial range, again modeled using the quasi-2D correlation scale from the TTM. The parameter $\alpha_{\perp}$ is taken to be equal to $1/\sqrt{3}$, after the test-particle simulations of W. H. Matthaeus et al. (2003), but it should be noted that this may be an overestimate of this quantity (see P. L. Els et al. 2024, and references therein). The above expression derives its rigidity dependence purely from those displayed by $\lambda_{\parallel}$, changing from a $P^{1/9}$ dependence at low rigidities, to a $P^{2/3}$ dependence at high rigidities.

Drifts due to gradients and curvatures of the large-scale Parker field (Equation (13)), as well as along a current sheet, are here, as in N. E. Engelbrecht et al. (2024), modeled following the approach proposed by R. A. Burger (2012; for alternative approaches employed in heliospheric GCR transport studies, see N. E. Engelbrecht et al. 2019; S. T. Mohlolo et al. 2022, and references therein). The current sheet is modeled using the expression proposed by J. Kota & J. R. Jokipii (1983), with the current sheet angle given by

$$\theta_{cs} = \frac{\pi}{2} - \tan^{-1}\left[\tan\alpha\,\sin\left(\frac{\Omega r}{V_{\rm sw}}\right)\right], \quad (18)$$

where it is assumed, for simplicity, that the tilt angle $\alpha = 0^{\circ}$, although this can be varied in future studies. The rotation rate Ω is again chosen to be equal to that of κ^1 Ceti. Previous astrospheric modulation studies (N. E. Engelbrecht et al. 2024; J. Light et al. 2025) assumed maximum drift effects, such that the drift coefficient is in the so-called weak-scattering limit (see M. A. Forman et al. 1974), such that $\kappa_A = vR_L/3$. It is, however, well established that high levels of turbulence would lead to a considerable reduction in drift effects (see, e.g., N. E. Engelbrecht et al. 2022, and references therein). In order to model this effect, an expression derived by N. E. Engelbrecht et al. (2017) is employed, given by

$$\kappa_A = \frac{vR_L}{3}\left[1 + \frac{\lambda_{\perp}^2}{R_L^2}\frac{\delta B_T^2}{B_0^2}\right]^{-1}, \quad (19)$$

with δB_T^2 denoting the total transverse variance. Use of this expression is motivated by its agreement with existing simulations (e.g., J. Minnie et al. 2007; R. C. Tautz & A. Shalchi 2012), as well as its successful implementation in heliospheric GCR modulation studies (e.g., N. E. Engelbrecht & K. D. Moloto 2021). We note, however, that recent test-particle simulations appear to indicate that Equation (19) may overestimate the influence of turbulence on particle drifts (see, e.g., P. L. Els et al. 2024; T. Laitinen & S. Dalla 2025). Therefore, GCR intensities calculated with this drift coefficient can be interpreted as reflecting a maximum effect of turbulence on particle drifts.

The left panel of Figure 3 shows the MFPs and drift length scales calculated using as inputs turbulence quantities yielded by the TTM at 1 au in the ecliptic plane, as functions of rigidity. I. D. Palmer (1982) consensus range values for $\lambda_{\parallel}$ and $\lambda_{\perp}$ at 1 u in the modern heliosphere are indicated by the green block and line, respectively, to give an idea as to modern values for these quantities (see also J. T. Lang et al. 2024). The parallel MFP remains mostly below the modern consensus range, as the lowering effect of the larger magnetic variance is balanced to some degree by the influence of larger values of the slab correlation scale, and displays a $P^{1/3}$ rigidity dependence. A combination of higher 2D variances and correlation scales leads to a perpendicular MFP significantly higher than what is expected in the modern heliosphere at 1 au, with the expected flatter $P^{1/9}$ rigidity dependence. Relatively high magnetic variances as well as a high perpendicular MFP lead to very small turbulence-reduced drift scales (dashed black line), relative to the weak-scattering values (solid black line). The right panel of Figure 3 shows the same MFPs and drift scales as functions of radial distance in the ecliptic plane, calculated at a rigidity of 1 GV. The parallel MFP increases steadily beyond 1 au, reflecting the decrease in the slab variance as function of radial distance seen in the top right panel of Figure 2. The perpendicular MFP displays a relatively flat radial dependence, approaching (but never exceeding) the parallel MFP at the smallest radial distances. Due to the high

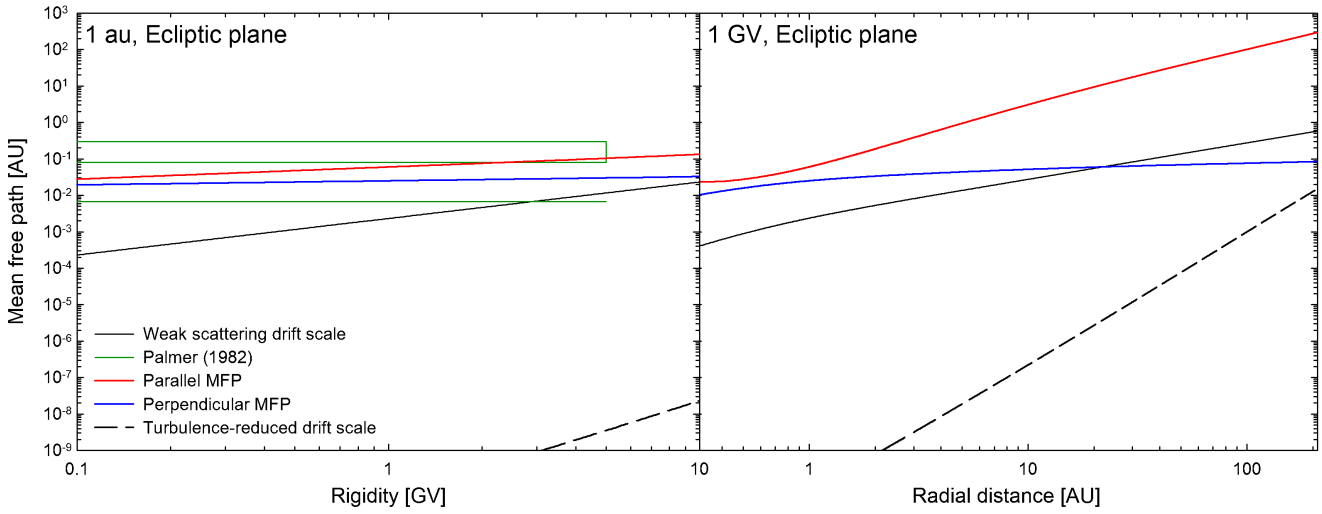

Figure 3. Left panel: parallel and perpendicular MFPs, as well as drift scales, at 1 au in the ecliptic plane as functions of rigidity, calculated using turbulence inputs for κ^1 Ceti. Right panel: the same, calculated at 1 GV as function of radial distance in the ecliptic plane. The modern heliospheric I. D. Palmer (1982) consensus range is indicated by the green lines. See text for details.

turbulence levels, the turbulence-reduced drift scale remains well below the weak-scattering values (which can exceed $\lambda_\perp$ beyond 30 au).

The LIS expression employed here is that of R. A. Burger et al. (2008), given by

$$j_B = \frac{19.0(P/P_0)^{-2.78}}{1.0 + (P/P_0)^{-2}}, \quad (20)$$

in units of $[\mathrm{m}^2\,\mathrm{sr\,s\,MeV}]^{-1}$, with $P_0 = 1$ GV. This LIS is scaled up by a factor of 2 in the Galactic spiral arms (Models 1 and 2), motivated by the scaling employed by H. Svensmark (2006a) based on star formation rates, as well as by the Galactic GCR transport studies of I. Büsching & M. S. Potgieter (2008), who report an increase by the same factor of the GCR flux within a Galactic spiral arm relative to outside it. The modulation boundary for each model is assumed to be at the corresponding TS location. Given the relatively limited extents of the astrosheath yielded by the various MHD simulations, not much modulation of GCRs is expected in this region, as opposed to what is observed in the modern heliosphere (see, e.g., E. C. Stone et al. 2013). Nevertheless, due to this assumption the differential intensities yielded by the modulation model should strictly be interpreted as representing an upper limit for the contribution of these particles to the radiation environment of the early Earth. The model boundary is here assumed to correspond to the TS locations for both models as listed in Table 2, thereby taking into account various, differing local interstellar conditions the Sun may have encountered in the distant past, and hence the influence of these changes on GCR modulation.

4.2. Galactic Cosmic-Ray Modulation Results

GCR proton differential intensities are calculated at 1 au as functions of kinetic energy, and are shown in Figure 4. Calculations are performed for both the weak-scattering drift coefficient (solid lines), and the turbulence-reduced drift coefficients (dashed lines). Modern heliospheric observations of GCR intensities at Earth reported by F. B. McDonald et al. (1992) are shown to guide the eye. Intensities calculated for the smaller astrosphere implied by the use of Model 2 tend to be larger than those computed for Model 1, this difference being more clearly seen for positive magnetic polarity conditions than for negative polarity conditions. Use of the weak-scattering drift coefficient leads to GCR intensities approximately an order of magnitude below modern observations (for both Models 1 and 2), with $A > 0$ intensities calculated for Model 2 approaching modern heliospheric observations during $A < 0$, in contrast with what is reported in previous studies. Intensities for Model 2 remain lower than those during the modern heliosphere, even though the TS radii are comparable, because the larger astrospheric magnetic field magnitude for κ^1 Ceti leads to smaller particle Larmor radii, and thus decreased drift effects. Solutions computed for $A > 0$ magnetic polarity conditions are larger than those for $A < 0$ polarity conditions at low and intermediate energies, with a crossover at higher energies, reminiscent of what is observed in the modern heliosphere (see, e.g., J. P. L. Reinecke & M. S. Potgieter 1994). This is due to the influence of the relatively fast rotation rate on the heliospheric magnetic field (HMF) geometry: the resulting highly wound HMF leads to the effective diffusion coefficient of GCRs being dominated by the perpendicular diffusion coefficient (see J. Light et al. 2025), while gradient and curvature drifts, which facilitate the inward transport of GCR protons over the poles during $A > 0$ (e.g., J. R. Jokipii & B. Thomas 1981), are more effective. The strong drift effects that can be seen in the weak-scattering results are greatly reduced in the turbulence-reduced case (dashed lines), reflecting the high (relative to the modern heliosphere) turbulence levels for κ^1 Ceti. For Model 2, the relatively smaller modulation volume does not lead to large GCR intensities: differential intensity spectra are approximately 3 orders of magnitude smaller than modern heliospheric observations, and are identical for both $A < 0$ and $A > 0$, indicative of a lack of drift effects. For Model 1, with a comparatively larger modulation volume, differential intensities are approximately 5 orders of magnitude smaller than modern observations. Interestingly, spectra for $A < 0$ are now larger than those computed for $A > 0$ conditions. There are two reasons for this. Beyond approximately 100 au, turbulence

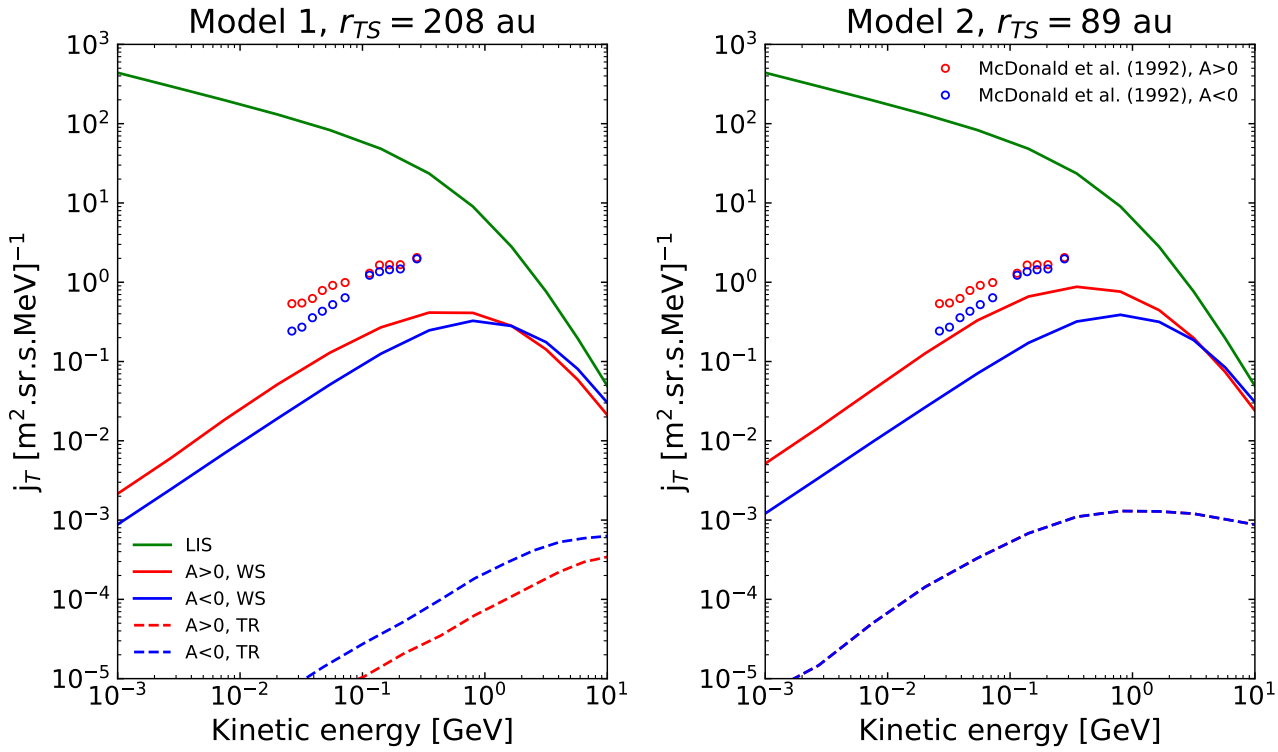

Figure 4. GCR proton differential intensities calculated at 1 au as functions of kinetic energy, for weak-scattering ("WS," solid lines) and turbulence-reduced ("TR," dashed lines) drift coefficients, for Model 1 (left panel) and Model 2 (right panel). The assumed LIS (Equation (20)) is indicated as the green lines. Also shown are heliospheric observations of GCR intensities at 1 au from F. B. McDonald et al. (1992), to provide perspective.

levels become small enough so that the drift coefficient is essentially equal to the weak-scattering value (Figure 3, right panel), which in turn becomes larger than the perpendicular diffusion coefficient, thereby allowing for drift effects to become significant. At higher latitudes, however, turbulence levels as modeled here are higher, leading to a greater reduction in the drift coefficient over the poles, thereby hampering the inward transport of GCR protons from the polar regions during $A > 0$.

5. Discussion

The present study represents the first attempt to model the transport of GCRs in an astrosphere other than the heliosphere, focusing on κ^1 Ceti, a young Sun proxy star, in order to ascertain whether GCRs could have comprised a significant proportion of the radiation environment at 1 au at an early stage of the Sun's evolution. Prior studies have argued that these particles did not. However, these employed simplified GCR transport models, and assumed very large astrospheric dimensions, implying a very large modulation volume that would inevitably lead to low GCR intensities. This latter assumption may not hold true, as the young Sun, in its orbit around the Galactic center, is expected to encounter a range of local interstellar conditions that will influence its dimensions, and hence the modulation volume of the early heliosphere. The present study investigates the influence of interstellar parameters expected in the Galactic spiral arms—regions of, for example, enhanced interstellar neutral densities—on the astrosphere of κ^1 Ceti.

Multifluid MHD simulations are essential in order to properly account for the physics governing the structures of astrospheres. For example, charge exchange processes play a significant role in mass, momentum, and energy loading, which in turn influence the ram pressure and thus the location of the TS. This directly influences the modulation volume of the astrosphere. Simulations of the astrosphere of κ^1 Ceti in the presence of two different states of LISM conditions expected to prevail within the Galactic spiral arms (Models 1 and 2) reveal an astrosphere considerably smaller than what would be expected from prior studies (where dimensions of the order of $\sim 10^3$ au are expected, see e.g., S. R. Raeside et al. 2025), despite the large mass-loss rate of this star, with the astrosphere yielded by Model 2 being comparable in dimensions to the modern heliosphere. This demonstrates the significance of the local interstellar environment in studies of different astrospheres, which is borne out by prior studies of the influence of varying LISM parameters on the modern heliosphere (see, e.g., H.-R. Müller et al. 2006; J. A. Miller & B. D. Fields 2022), and highlights the importance of properly taking into account the local interstellar context when engaged in the MHD modeling of different astrospheres, which due to their unique locations in the Galactic context can be influenced by a broad range of local interstellar factors. We also demonstrate that analytical approaches to calculating the location of the TS of a given astrosphere can be quite inaccurate when compared with the results of full multifluid MHD simulations, and we recommend caution when such approximations are employed in the context of GCR modulation studies.

In order to model the evolution of turbulence parameters essential to the calculation of GCR diffusion coefficients throughout the astrosphere, we employ for the first time a TTM within an astrospheric context, this being the steady-state two-component model proposed by S. Oughton et al. (2011), motivated by its successful use in heliospheric GCR transport

studies (see, e.g., N. E. Engelbrecht & R. A. Burger 2013a). This model is solved for prespecified large-scale fields using input parameters from the MHD results for Models 1 and 2 (i.e., astrospheric dimensions, magnetic field magnitude and geometry, stellar wind speed, and proton density), and inner boundary values that are scaled from heliospheric values reported by N. E. Engelbrecht & R. D. T. Strauss (2018) based on observations reported on by V. S. Airapetian et al. (2021). The picture that emerges is that of an astrosphere characterized by turbulence levels (as quantified by predicted magnetic variances) significantly higher than those observed in the modern heliosphere, as well as larger magnetic correlation lengths. It is interesting to note that the radial dependences of these quantities, when the turbulence generated through pickup-ion formation is neglected, is very similar to that predicted for the heliosphere by the TTM under the same assumption (see, e.g., N. E. Engelbrecht & R. A. Burger 2015b), as well as similar to what is observed in the heliosphere (e.g., M. E. Cuesta et al. 2022; R. A. Burger & S. R. McKee 2023).

The results of the abovementioned TTM are then used as direct inputs for the 3D GCR modulation model of N. E. Engelbrecht et al. (2024). GCR intensities computed at 1 au clearly demonstrate the importance of the drift mechanism in the inward transport of these particles. Both Models 1 and 2, corresponding to very different modulation volumes, use weak-scattering (or maximum) drift coefficients, which leads to GCR intensities relatively close to, but still smaller than, those observed in the modern heliosphere. However, modeling the reducing influence of turbulence on GCR drift coefficients leads to significantly lower GCR intensities, more in line with what is reported in previous studies (e.g., S. R. Raeside et al. 2025), albeit somewhat higher. This can be understood as an effect of the combination of the enhanced turbulence levels as well as the high rotation speed observed for κ^1 Ceti, which leads to a highly wound astrospheric magnetic field. This means that the inward radial transport of GCRs would predominantly depend on the perpendicular and drift coefficients. The high turbulence levels expected for κ^1 Ceti (as modeled here) lead to a correspondingly high perpendicular diffusion coefficient (an effect somewhat ameliorated by the larger astrospheric magnetic field magnitude), but would also lead to a significant reduction in the drift coefficient, thereby effectively removing one of the mechanisms whereby GCRs can be effectively transported into the astrosphere. It should be noted that the choice of other transport coefficients can reduce this effect, as for example other scattering theories can yield larger perpendicular diffusion coefficients for a given set of turbulence parameters (see, e.g., N. E. Engelbrecht et al. 2022). As a first approach, a combination of diffusion and turbulence-reduced drift coefficients were used in this study that in prior studies have been able to reproduce GCR intensities in the heliosphere. In subsequent studies, the influence of the choice of transport coefficients will be investigated in more detail, with choices of theories motivated by direct numerical test-particle simulations of diffusion (and drift) coefficients (such as those performed by P. L. Els et al. 2024) in turbulence conditions such as those yielded by the TTM. Nevertheless, this result highlights the importance of a 3D treatment of GCR transport within astrospheres: lower-dimensional transport models simply cannot realistically take into account the interplay of anisotropic diffusion and drift that governs the transport of these particles.

The physics-first modeling approach introduced here will also in subsequent studies be employed to model the radiation environments of a range of different exoplanet-hosting astrospheres, as well as for various proxies for different developmental stages of the Sun such as EK Draconis. This approach will provide new insights as to the extremely long-term evolution of the Earth's ionizing radiation environments and hence on the habitability of (exo)planetary systems. This is particularly important in the context of studying the transport of energetic particles of solar or stellar origin as well as those originating from gamma-ray bursts, as these can also have important implications for the chemistry of protoplanetary disks (C. Rab et al. 2017) as well as prebiotic chemistry (K. Kobayashi et al. 2023). The insights provided by this study as to the transport coefficients of these particles will prove invaluable in such future studies.

Acknowledgments

This research was supported in part by the International Space Science Institute (ISSI) in Bern, through ISSI International Team project No. 24-608. K.H. acknowledges financial support from the Research Council of Norway (RCN), through its Centre of Excellence funding scheme, project No. 332523 (PHAB, Centre for Planetary Habitability). V.S.A. acknowledges support from the NASA/GSFC Sellers Exoplanet Environments Collaboration (SEEC), which is funded by the NASA Planetary Science Division's Internal Scientist Funding Model (ISFM), NASA's Astrophysics Theory Program grant #80NSSC24K0776, and NASA XRP grant #80NSSC22K0674.

Software: CRONOS (R. Kissmann et al. 2018; K. Scherer et al. 2025), Matplotlib (J. D. Hunter 2007), NumPy (C. R. Harris et al. 2020).

Author Contribution

All authors contributed equally to the manuscript.

ORCID iDs

N. Eugene Engelbrecht https://orcid.org/0000-0003-3659-7956
Konstantin Herbst https://orcid.org/0000-0001-5622-4829
Klaus Scherer https://orcid.org/0000-0002-9530-1396
Sean Oughton https://orcid.org/0000-0002-2814-7288
Vladimir S. Airapetian https://orcid.org/0000-0003-4452-0588

References

Adhikari, L., Zank, G. P., Telloni, D., et al. 2017, ApJ, 851, 117
Adhikari, L., Zank, G. P., & Zhao, L. 2021, Fluids, 6, 368
Airapetian, V. S., Glocer, A., Gronoff, G., Hébrard, E., & Danchi, W. 2016, NatGe, 9, 452
Airapetian, V. S., Glocer, A., Khazanov, G. V., et al. 2017, ApJL, 836, L3
Airapetian, V. S., Barnes, R., Cohen, O., et al. 2020, IJAsB, 19, 136
Airapetian, V. S., Jin, M., Lüftinger, T., et al. 2021, ApJ, 916, 96
Airapetian, V. S., & Usmanov, A. V. 2016, ApJL, 817, L24
Amato, E., & Blasi, P. 2018, AdSpR, 62, 2731
Armillotta, L., Ostriker, E. C., & Linzer, N. B. 2025, ApJ, 989, 140
Bavassano, B., Pietropaolo, E., & Bruno, R. 2000a, JGR, 105, 12697
Bavassano, B., Pietropaolo, E., & Bruno, R. 2000b, JGR, 105, 15959
Bishop, M. A., Oughton, S., Parashar, T. N., & Perrott, Y. C. 2025, ApJ, 979, 211
Breech, B., Matthaeus, W. H., Minnie, J., et al. 2005, GeoRL, 32, L06103

Breech, B., Matthaeus, W. H., Minnie, J., et al. 2008, JGR, 113, A08105
Breitschwerdt, D., & de Avillez, M. A. 2006, A&A, 452, L1
Burger, R. A. 2012, ApJ, 760, 60
Burger, R. A., & McKee, S. R. 2023, AdSpR, 71, 4916
Burger, R. A., Krüger, T. P. J., Hitge, M., & Engelbrecht, N. E. 2008, ApJ, 674, 511
Burger, R. A., Nel, A. E., & Engelbrecht, N. E. 2022, ApJ, 926, 128
Büsching, I., & Potgieter, M. S. 2008, AdSpR, 42, 504
Callingham, J. R., Tasse, C., Keers, R., et al. 2025, Natur, 647, 603
Castro-Ginard, A., McMillan, P. J., Luri, X., et al. 2021, A&A, 652, A162
Cohen, O., Drake, J. J., & Kóta, J. 2012, ApJ, 760, 85
Cuesta, M. E., Chhiber, R., Roy, S., et al. 2022, ApJL, 932, L11
do Nascimento, J. D., Jr., Vidotto, A. A., Petit, P., et al. 2016, ApJL, 820, L15
Draine, B. T. 2011, Physics of the Interstellar and Intergalactic Medium (Princeton University Press)
Els, P. L., Engelbrecht, N. E., Lang, J. T., & Strauss, R. D. 2024, ApJ, 975, 134
Engelbrecht, N. E. 2017, ApJL, 849, L15
Engelbrecht, N. E. 2024, ApJ, 975, 227
Engelbrecht, N. E., & Burger, R. A. 2013a, ApJ, 772, 46
Engelbrecht, N. E., & Burger, R. A. 2013b, ApJ, 779, 158
Engelbrecht, N. E., & Burger, R. A. 2015a, ApJ, 814, 152
Engelbrecht, N. E., & Burger, R. A. 2015b, AdSpR, 55, 390
Engelbrecht, N. E., & Moloto, K. D. 2021, ApJ, 908, 167
Engelbrecht, N. E., & Strauss, R. D. T. 2018, ApJ, 856, 159
Engelbrecht, N. E., & Di Felice, V. 2020, PhRvD, 102, 103007
Engelbrecht, N. E., Strauss, R. D., le Roux, J. A., & Burger, R. A. 2017, ApJ, 841, 107
Engelbrecht, N. E., Mohlolo, S. T., & Ferreira, S. E. S. 2019, ApJL, 884, L54
Engelbrecht, N. E., Effenberger, F., Florinski, V., et al. 2022, SSRv, 218, 33
Engelbrecht, N. E., Herbst, K., Strauss, R. D. T., et al. 2024, ApJ, 964, 89
Evensberget, D., Marsden, S. C., Carter, B. D., et al. 2023, MNRAS, 524, 2042
Fisk, L. A. 1996, JGR, 101, 15547
Forman, M. A., Jokipii, J. R., & Owens, A. J. 1974, ApJ, 192, 535
Forsyth, R. J., Horbury, T. S., Balogh, A., & Smith, E. J. 1996, GeoRL, 23, 595
Fraschetti, F., Alvarado-Gómez, J. D., Drake, J. J., Cohen, O., & Garraffo, C. 2022, ApJ, 937, 126
Frisch, P. C., & Mueller, H.-R. 2013, SSRv, 176, 21
Fuchs, B., Breitschwerdt, D., de Avillez, M. A., & Dettbarn, C. 2009, SSRv, 143, 437
Globus, N., & Blandford, R. D. 2020, ApJL, 895, L11
Güdel, M. 2007, LRSP, 4, 3
Harris, C. R., Millman, K. J., van der Walt, S. J., et al. 2020, Natur, 585, 357
Herbst, K. 2013, PhD thesis, Kiel https://macau.uni-Kiel.de/receive/diss_mods_00010634
Herbst, K., Grenfell, J. L., Sinnhuber, M., et al. 2019, A&A, 631, A101
Herbst, K., Scherer, K., Ferreira, S. E. S., et al. 2020, ApJL, 897, L27
Herbst, K., Baalmann, L., Bykov, A., et al. 2022, SSRv, 218, 29
Herbst, K., Bartenschlager, A., Grenfell, J. L., et al. 2024, ApJ, 961, 164
Hill, M. L., Bott, K., Dalba, P. A., et al. 2023, AJ, 165, 34
Hu, J., Airapetian, V. S., Li, G., Zank, G., & Jin, M. 2022, SciA, 8, eabi9743
Hunter, J. D. 2007, CSE, 9, 90
Iovieno, M., Gallana, L., Fraternale, F., et al. 2016, EuJMB, 55, 394
Isenberg, P. A., Smith, C. W., & Matthaeus, W. H. 2003, ApJ, 592, 564
Jasinski, J. M., Nordheim, T. A., Hasegawa, Y., & Murphy, N. 2020, ApJL, 899, L18
Jokipii, J. R. 1966, ApJ, 146, 480
Jokipii, J. R., & Thomas, B. 1981, ApJ, 243, 1115
Kammerer, J., Quanz, S. P., Dannert, F. & the LIFE Collaboration 2022, A&A, 668, A52
Kissmann, R., Kleimann, J., Krebl, B., & Wiengarten, T. 2018, ApJS, 236, 53
Kleimann, J., Oughton, S., Fichtner, H., & Scherer, K. 2023, ApJ, 953, 133
Kobayashi, K., Ise, J.-i., Aoki, R., et al. 2023, Life, 13, 1103
Kóta, J. 2016, JPhCS, 767, 012014
Kota, J., & Jokipii, J. R. 1983, ApJ, 265, 573
Laitinen, T., & Dalla, S. 2025, ApJ, 979, 106
Lang, J. T., Strauss, R. D., Engelbrecht, N. E., et al. 2024, ApJ, 971, 105
Leung, H. W., Bovy, J., Mackereth, J. T., et al. 2023, MNRAS, 519, 948
Light, J., Ferreira, S. E. S., Engelbrecht, N. E., Scherer, K., & Herbst, K. 2022, MNRAS, 516, 3284
Light, J., Engelbrecht, N. E., Herbst, K., & Scherer, K. D. 2025, MNRAS, 537, 2097
Linsky, J. 2014, Chall, 5, 351
Linsky, J. L., & Moebius, E. 2023, ApJ, 942, 45
Maehara, H., Shibayama, T., Notsu, S., et al. 2012, Natur, 485, 478
Matthaeus, W. H., Oughton, S., Pontius, D., & Zhou, Y. 1994, JGR, 99, 19267
Matthaeus, W. H., Smith, C. W., & Bieber, J. W. 1999, AIPC, 471, 511
Matthaeus, W. H., Qin, G., Bieber, J. W., & Zank, G. P. 2003, ApJ, 590, L53
McDonald, F. B., Moraal, H., Reinecke, J. P. L., Lal, N., & McGuire, R. E. 1992, JGR, 97, 1557
Mesquita, A. L., Rodgers-Lee, D., & Vidotto, A. A. 2021, MNRAS, 505, 1817
Miller, J. A., & Fields, B. D. 2022, ApJ, 934, 32
Minnie, J., Bieber, J. W., Matthaeus, W. H., & Burger, R. A. 2007, ApJ, 670, 1149
Mohlolo, S. T., Engelbrecht, N. E., & Ferreira, S. E. S. 2022, AdSpR, 69, 2574
Moloto, K. D., Engelbrecht, N. E., & Burger, R. A. 2018, ApJ, 859, 107
Moloto, K. D., Engelbrecht, N. E., Strauss, R. D., Moeketsi, D. M., & van den Berg, J. P. 2019, AdSpR, 63, 626
Müller, H.-R., Frisch, P. C., Florinski, V., & Zank, G. P. 2006, ApJ, 647, 1491
Müller, H. R., Frisch, P. C., Fields, B. D., & Zank, G. P. 2009, SSRv, 143, 415
Namekata, K., Maehara, H., Honda, S., et al. 2021, NatAs, 6, 241
Namekata, K., Airapetian, V. S., Petit, P., et al. 2024a, ApJ, 961, 23
Namekata, K., Ikuta, K., Petit, P., et al. 2024b, ApJ, 976, 255
Namekata, K., Maehara, H., Notsu, Y., et al. 2025, ApJ, 993, 80
Notsu, Y., Maehara, H., Honda, S., et al. 2019, ApJ, 876, 58
Obridko, V. N., Ragulskaya, M. V., & Khramova, E. G. 2020, JASTP, 208, 105395
Okamoto, S., Notsu, Y., Maehara, H., et al. 2021, ApJ, 906, 72
Opher, M., Loeb, A., & Peek, J. E. G. 2024, NatAs, 8, 983
Oughton, S., Dmitruk, P., & Matthaeus, W. H. 2006, PhPl, 13, 042306
Oughton, S., Matthaeus, W. H., Smith, C. W., Breech, B., & Isenberg, P. A. 2011, JGRA, 116, A08105
Oughton, S., & Engelbrecht, N. E. 2021, NewA, 83, 101507
Palmer, I. D. 1982, RvGSP, 20, 335
Parker, E. N. 1958, ApJ, 128, 664
Parker, E. N. 1963, Interplanetary Dynamical Processes (Interscience Publishers)
Parker, E. N. 1965, P&SS, 13, 9
Pei, C., Bieber, J. W., Breech, B., et al. 2010, JGR, 115, A03103
Perri, S., & Balogh, A. 2010, GeoRL, 37, L17102
Pezzi, O., & Blasi, P. 2024, MNRAS, 529, L13
Poppenhaeger, K. 2022, MNRAS, 512, 1751
Rab, C., Güdel, M., Padovani, M., et al. 2017, A&A, 603, A96
Raeside, S. R., Rodgers-Lee, D., & Rimmer, P. B. 2025, A&A, 697, A26
Ragulskaya, M. V., Khramova, E. G., & Obridko, V. N. 2018, Ge&Ae, 58, 877
Rauer, H., Aerts, C., Cabrera, J., et al. 2025, ExA, 59, 26
Reinecke, J. P. L., & Potgieter, M. S. 1994, JGR, 99, 14761
Roberts, D. A., Goldstein, M. L., Klein, L. W., & Matthaeus, W. H. 1987, JGR, 92, 12023
Rodgers-Lee, D., Vidotto, A. A., Taylor, A. M., Rimmer, P. B., & Downes, T. P. 2020, MNRAS, 499, 2124
Rodgers-Lee, D., Taylor, A. M., Vidotto, A. A., & Downes, T. P. 2021a, MNRAS, 504, 1519
Rodgers-Lee, D., Vidotto, A. A., & Mesquita, A. L. 2021b, MNRAS, 508, 4696
Rodgers-Lee, D., Rimmer, P. B., Vidotto, A. A., et al. 2023, MNRAS, 521, 5880
Rucinski, S. M., Walker, G. A. H., Matthews, J. M., et al. 2004, PASP, 116, 1093
Scherer, K., Fichtner, H., Borrmann, T., et al. 2006, SSRv, 127, 327
Scherer, K., Fichtner, H., Heber, B., Ferreira, S. E. S., & Potgieter, M. S. 2008, AdSpR, 41, 1171
Scherer, K., Fichtner, H., Fahr, H. J., Bzowski, M., & Ferreira, S. E. S. 2014, A&A, 563, A69
Scherer, K., van der Schyff, A., Bomans, D. J., et al. 2015, A&A, 576, A97
Scherer, K., Herbst, K., Engelbrecht, N. E., et al. 2025, A&A, 694, A106
Scheucher, M., Herbst, K., Schmidt, V., et al. 2020, ApJ, 893, 12
Schulreich, M. M., Breitschwerdt, D., Feige, J., & Dettbarn, C. 2018, Galax, 6, 26
Shalchi, A. 2009, ASSL, 362
Shalchi, A., Bieber, J. W., & Matthaeus, W. H. 2004, ApJ, 604, 675
Shaviv, N. J. 2002, PhRvL, 89, 051102
Shields, A. L., Ballard, S., & Johnson, J. A. 2016, PhR, 663, 1
Smith, C. W., Matthaeus, W. H., Zank, G. P., et al. 2001, JGR, 106, 8253
Smith, C. W., Isenberg, P. A., Matthaeus, W. H., & Richardson, J. D. 2006, ApJ, 638, 508
Steyn, P. J., & Burger, R. A. 2020, ApJ, 902, 33
Stone, E. C., Cummings, A. C., McDonald, F. B., et al. 2013, Sci, 341, 150
Strauss, R. D. T., & Effenberger, F. 2017, SSRv, 212, 151

Svensmark, H. 2006a, AN, 327, 871
Svensmark, H. 2006b, AN, 327, 866
Tabataba-Vakili, F., Grenfell, J. L., Grießmeier, J. M., & Rauer, H. 2016, A&A, 585, A96
Tautz, R. C., & Shalchi, A. 2012, ApJ, 744, 125
Teufel, A., & Schlickeiser, R. 2003, A&A, 397, 15
Troskie, J. S., Engelbrecht, N. E., & Steyn, P. J. 2024, ApJ, 970, 144
Usmanov, A. V., Goldstein, M. L., & Matthaeus, W. H. 2012, ApJ, 754, 40
Usmanov, A. V., Goldstein, M. L., & Matthaeus, W. H. 2016, ApJ, 820, 17
Usmanov, A. V., Chhiber, R., Matthaeus, W. H., Roy, S., & Goldstein, M. L. 2025, ApJ, 993, 87
Veronig, A. M., Dissauer, K., Kliem, B., et al. 2025, LRSP, 22, 2
Vidotto, A. A. 2021, LRSP, 18, 3
Vidotto, A. A., Opher, M., Jatenco-Pereira, V., & Gombosi, T. I. 2009, ApJ, 699, 441
Weygand, J. M., Matthaeus, W. H., Dasso, S., et al. 2009, JGRA, 114, A07213
Weygand, J. M., Matthaeus, W. H., Dasso, S., & Kivelson, M. G. 2011, JGR, 116, A08102
Wiengarten, T., Oughton, S., Engelbrecht, N. E., et al. 2016, ApJ, 833, 17
Wilkin, F. P. 2000, ApJ, 532, 400
Williams, L. L., & Zank, G. P. 1994, JGR, 99, 19229
Wyman, K., & Redfield, S. 2013, ApJ, 773, 96
Youngblood, A., France, K., Koskinen, T., et al. 2025, AJ, 170, 342
Zank, G. P., & Frisch, P. C. 1999, ApJ, 518, 965
Zank, G. P., Matthaeus, W. H., & Smith, C. W. 1996, JGR, 101, 17093
Zank, G. P., Rice, W. K. M., & Wu, C. C. 2000, JGR, 105, 25079
Zank, G. P., Dosch, A., Hunana, P., et al. 2012, ApJ, 745, 35
Zank, G. P., Adhikari, L., Hunana, P., et al. 2017, ApJ, 835, 147
Zank, G. P., Sterken, V., Giacalone, J., et al. 2022, SSRv, 218, 34
Zhao, L. L., Adhikari, L., Zank, G. P., Hu, Q., & Feng, X. S. 2018, ApJ, 856, 94
Zucker, C., Goodman, A. A., Alves, J., et al. 2022, Natur, 601, 334